Multifunctional Sn- and Fe-Codoped In2O3 Colloidal Nanocrystals: Plasmonics and Magnetism

3 AUTHORS:

Bharat Tandon

Indian Institute of Science Education and Res…

3 PUBLICATIONS **10** CITATIONS

SEE PROFILE

G Shiva Shanker

Indian Institute of Science Education and Res…

5 PUBLICATIONS **20** CITATIONS

SEE PROFILE

Angshuman Nag

Indian Institute of Science Education and Res…

44 PUBLICATIONS **1,497** CITATIONS

SEE PROFILE

Multifunctional Sn- and Fe-Codoped In$_2$O$_3$ Colloidal Nanocrystals: Plasmonics and Magnetism

Bharat Tandon, G. Shiva Shanker, and Angshuman Nag*

Department of Chemistry, Indian Institute of Science Education and Research (IISER), Pune 411008, India

Ⓢ Supporting Information

ABSTRACT: We prepared Fe- and Sn-codoped colloidal In$_2$O$_3$ nanocrystals (∼6 nm). Sn doping provides free electrons in the conduction band, originating localized surface plasmon resonance (LSPR) and electrical conductivity. The LSPR band can be tuned between 2000 and >3000 nm, depending on the extent and kind of dopant ions. Fe doping, on the other hand, provides unpaired electrons, resulting in weak ferromagnetism at room temperature. Fe doping shifts the LSPR band of 10% Sn-doped In$_2$O$_3$ nanocrystals to a longer wavelength along with a reduction in intensity, suggesting trapping of charge carriers around the dopant centers, whereas Sn doping increases the magnetization of 10% Fe-doped In$_2$O$_3$ nanocrystals, probably because of the free electron mediated interactions between distant magnetic ions. The combination of plasmonics and magnetism, in addition to electronic conductivity and visible-light transparency, is a unique feature of our colloidal codoped nanocrystals.

SECTION: Physical Processes in Nanomaterials and Nanostructures
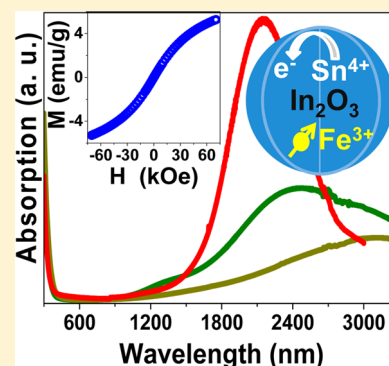
The Sn^{4+}-doped In$_2$O$_3$ (ITO) compound is a benchmark transparent conducting oxide (TCO) that can simultaneously conduct electricity and is transparent to visible light. Colloidal ITO nanocrystals (NCs) have been explored recently exhibiting intense localized surface plasmon resonance (LSPR) band in the near- to mid-infrared region.[1−5] Here, we add another functionality, namely magnetic properties, by codoping Fe and Sn in to In$_2$O$_3$ (Fe-doped ITO) NCs. Furthermore, the magnetic property can be tuned by the plasmonic dopant (Sn), and the plasmonic property can be tuned by the magnetic dopant (Fe) ion.

Multifunctionality in a single NC is generally achieved either by forming heterostructured NCs or by doping the NC lattice/surface with impurities.[6−8] Search for the combination of near-infrared (NIR) plasmonic and magnetic property in solution processed NCs has gained momentum in recent times, especially for photothermal therapy for selective treatment of tumor cells.[9−12] Magnetic properties make the NC a good contrast agent for magnetic resonance imaging (MRI), and the absorbed NIR radiation by the same NC can be converted to heat causing the localized destruction of the diseased cell. Heterostructured NCs or nanocomposites, for example, Fe$_3$O$_4$/Au[9] and Fe$_3$O$_4$/Cu$_{2−x}$S[12] core/shell NCs have been demonstrated where the core exhibits magnetic properties and the shell exhibits plasmonic properties. Significant interactions have not been observed between the properties of such core and shell materials. To the best of our knowledge, there is no example of doped NCs that can simultaneously exhibit both magnetic and plasmonic properties.

We chose to codope Fe^{3+} and Sn^{4+} into In$_2$O$_3$ NC lattice. Fe^{3+} with five unpaired electrons can yield magnetism, and Sn^{4+} forms shallow electron donor states yielding free electrons in

the conduction band of In$_2$O$_3$. The LSPR frequency of our doped NC can be controlled over a range of 2000 to over 3000 nm by controlling the extent of doping. Such a range of tuning in LSPR frequency results from change in free electron concentration controlled by dopant concentrations and cannot be achieved from LSPR of metal NCs.[13] Previously discussed multifunctional heterostructured NCs like Fe$_3$O$_4$/Au core/shell ones do not exhibit LSPR within such wavelength range. In order to achieve NIR (typically <1000 nm) LSPR using Au based nanostructures, large dimensions (>50 nm) of Au is required, which is not desirable for *in vivo* biological applications.

On the other hand, Fe-doped In$_2$O$_3$ is a dilute magnetic semiconductor.[14] Sn codoping in the lattice of Fe-doped In$_2$O$_3$ adds free electrons, which in turn can facilitate magnetic interactions between Fe^{3+} ions that are more often far from each other in the NC lattice because of the dilute (<10%) level of doping. Interestingly, our preliminary results suggest possible interplay between the two different kinds of dopants: (i) Fe doping shifting LSPR band arising from Sn dopant toward longer wavelength, and (ii) Sn doping enhancing magnetic interactions between magnetic ions.

Table 1 shows the elemental analysis for a series of Fe-doped ITO nanocrystals using both inductively coupled plasma optical emission spectroscopy (ICP−OES) and energy-dispersive X-ray analysis (EDAX). Representative EDAX spectra are shown in Figure S1 of the Supporting Information. It was found that

Table 1. Elemental Analysis of Fe and Sn Codoped In_2O_3 NCs Using Both ICP-OES and EDAX

	In:Fe:Sn (atomic %)	
precursor	ICP-OES	EDAX
95:5: 0	94.3:5.7:0	95.3:4.7:0
90:10:0	88.8:11.2:0	90.5:9.5:0
95:0: 5	94.5:0: 5.5	94.8:0: 5.2
90:0: 10	89.5:0: 10.5	90.9:0: 9.1
90:5: 5	90.2:4.8:5.0	89.3:5.1:5.6
85:10:5	83.9:10.8:5.3	86.3:8.9:4.8
85:5: 10	83.6:5.5:10.9	85.6:4.8:9.6
80:10:10	79.0:10.4:10.6	81.4:9.0:9.6

for all compositions, In:Fe:Sn measured using both the techniques were similar to the precursor ratios. So, the precursor concentrations will be mentioned for all further discussion in this report. We note here that the high efficacy of doping Sn or Fe in In_2O_3 NCs is similar to prior literature reporting high level (>10%) of doping in similar systems.[1,2]

Figure 1a and Figure S2 of Supporting Information compares powder X-ray diffraction (XRD) for Fe and Sn-doped In_2O_3
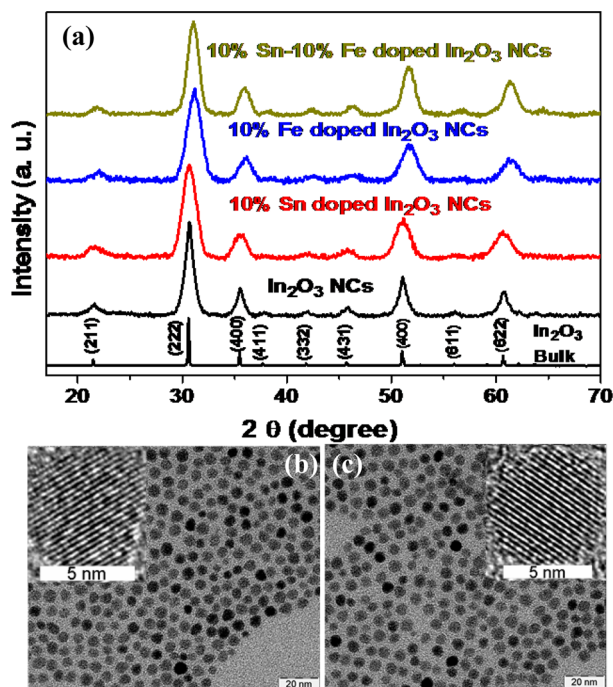
Figure 1. (a) Powder XRD patterns of In_2O_3 NCs, 10% Sn-doped In_2O_3 NCs, 10% Fe-doped NCs and 10% Sn−10% Fe-codoped In_2O_3 NCs. JCPDS (88-2160, space group $Ia3$) data for bulk In_2O_3 with cubic bixbyite phase is shown as reference. TEM image of (b) 10% Sn-doped In_2O_3 NCs and (c) 10% Sn−10% Fe-codoped In_2O_3 NCs. Insets to Figure 1b and 1c shows HRTEM image of a NC for the corresponding sample.

NCs with varying dopant concentrations. Clearly, XRD patterns of all the doped and undoped NCs matches with that of the cubic bixbyite of bulk In_2O_3 (JCPDS no. 88-2160, space group $Ia3$). No impurity peak corresponding to metallic Fe and Sn and their oxides are observed, suggesting a phase-pure sample. Supporting Information Figure S2a shows that the lattice parameters of all Sn-doped In_2O_3 NCs remains similar to that of undoped NCs. This similarity in lattice parameters is

because of the similar ionic radius of Sn^{4+} and In^{3+} ions and agrees with prior reports of ITO NCs.[15] However, lattice parameters shift systematically after doping Fe into the In_2O_3 NC lattice (Supporting Information Figure S2b). Ionic radius of Fe^{3+} is smaller than that of In^{3+}, consequently, XRD peaks shifts toward larger 2θ values, signifying smaller interplanar distances (smaller unit cell) for Fe-doped NCs. Figure 1a, keeping consistency with Supporting Information Figure S2, shows that 10% Sn-doped and undoped In_2O_3 NCs exhibit similar lattice parameters, whereas both 10% Fe-doped and 10% Sn−10% Fe-codoped NCs exhibit lattice parameters smaller than the host In_2O_3 NCs. All XRD data show that the lattice parameters of NCs does not change with Sn doping (Figure S3a in Supporting Information); however, lattice parameters decrease systematically with Fe doping (Figure S3b in Supporting Information).

Transmission electron microscopy (TEM) images in Figure 1b and c show nearly spherical particles with similar average diameters of 6.3 and 6.1 nm for both 10% Sn-doped In_2O_3 and 10% Sn−10% Fe-codoped In_2O_3 NCs, respectively. Likewise, 10% Fe-doped In_2O_3 NCs exhibit an average diameter of 5.9 nm (Figure S4 in Supporting Information). However, the undoped In_2O_3 NCs prepared under similar reaction conditions are larger, with an average diameter 9 nm. Larger crystallite size of undoped NCs was also reflected by narrower XRD peaks in Figure 1a, Supporting Information Figure S2 and Figure S3. Influence of dopant ion in the growth of doped In_2O_3 was also observed previously,[4] though the mechanism is not yet understood. High resolution TEM (HRTEM) images exhibit single crystalline nature for undoped In_2O_3 NCs (Figure S5 in Supporting Information), 10% Sn-doped In_2O_3 NCs (inset to Figure 1b), 10% Fe-doped NCs (inset to Figure S4 in Supporting Information), and 10% Sn−10% Fe-codoped In_2O_3 NCs (inset to Figure 1c). The obtained interplanar distances from HRTEM images are 2.93 Å for both In_2O_3 and 10% Sn-doped In_2O_3 NCs corresponding to (222) plane of In_2O_3 in cubic bixbite phase. The (222) interplanar distance decreases to 2.86 Å for both 10% Fe-doped In_2O_3 NCs and 10% Sn−10% Fe-codoped In_2O_3 NCs owing to the smaller size of Fe^{3+} ions compared to both In^{3+} and Sn^{4+} ion. Reduction of interplanar distance in single NC HRTEM measurements after incorporation of smaller Fe^{3+} ions in the lattice agrees well with our ensemble XRD measurements in Figure 1a. A careful investigation of interplanar distances of a large number of HRTEM images across different NC samples shows no other impurity phase apart from In_2O_3 related NCs. Also, the homogeneity in NC size/morphology for all samples observed in TEM images (Figure 1b and c and Supporting Information Figure S4), and also in scanning electron microscopy (SEM) image (Supporting Information Figure S6) showing a larger area, suggests only one kind of NC.

Bandgap of bulk In_2O_3 with bixbyite structure has been debated. Ref 16 has recently suggested that the low-intensity absorption edge at 2.93 eV is the direct bandgap separating the valence band maximum (VBM) and the conduction band minimum (CBM); however, the optical transition is forbidden within the dipole approximation due to the symmetry of the bixbyite crystal structure. Instead, a strong optical absorption is observed at higher energies ~3.55 eV, termed as optical gap, obtained by extrapolating the leading edge to the baseline.[16] Figure S7 in Supporting Information shows optical gap of our colloidal In_2O_3 NCs with average diameter 9 nm is 3.6 eV. Size-dependent bandgap tuning is not observed, because our NCs

are larger compared to the calculated Bohr excitonic radius (2.13 nm)[15] of In_2O_3. Figure 2a shows that the optical gap
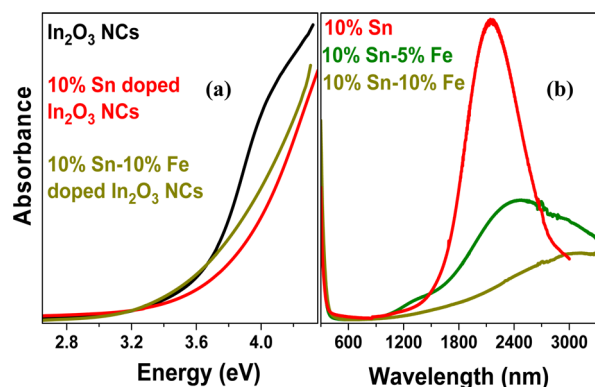

Figure 2. UV−visible−NIR absorption spectra of doped and undoped In_2O_3 NCs. (a) Optical gap of the NCs in the UV region. Spectrum of 10% Sn−5% Fe-codoped NCs is similar to that of 10% Sn−10% Fe-doped NCs, and therefore has not been shown here for clarity. (b) LSPR bands in the NIR to mid-IR region. Undoped In_2O_3 NCs do not show LSPR peak in this spectra region. NCs were dispersed in tetrachloroethylene solvent.

shifts to higher energies by doping Sn in to the In_2O_3 lattice. Similar widening of the gap was observed earlier and was attributed to the Burstein−Moss effect.[4,15] However, incorporating Fe into the lattice of Sn-doped In_2O_3 NCs shifts the gap toward lower energy (Figure 2a). Similar narrowing of gap was

observed previously after doping Fe in both In_2O_3 and Sn-doped In_2O_3 and was attributed to the many-body effect of free carriers;[14] however, a detailed study of band structure for these doped NCs is required. Another interesting observation in Figure 2a is the bleaching of excitonic feature with Sn doping. TEM data shows that ITO NCs are somewhat smaller than the undoped In_2O_3 NCs and no clear difference in size distribution is observed between the doped and undoped samples. So, consideration of larger size and broader size distribution cannot explain the bleaching of excitonic absorption feature in the doped NC. Instead, the excitonic bleaching in doped NCs could be attributed to the same free electrons in the conduction-band originating LSPR. The free-electron plasma in Sn-doped NCs screens the electron−hole Coulomb attraction required to form an excitonic state. Similar bleaching of excitonic absorption was previously observed for charged ZnO NCs with free-electrons in conduction-band.[17,18]

Figure 2b shows the tuning of LSPR band with variation of dopant content. Undoped In_2O_3 NCs do not show any LSPR band in this spectral region. As the number of free electrons increases with Sn doping in In_2O_3 NCs, the LSPR band shifts toward lower wavelength and become more intense (Figure S8 of Supporting Information) up to 10% Sn concentration, similar to Drude model. It is to be noted that Gamelin et al. observed deviation from Drude model while explaining the LSPRs of charged ZnO,[19] but still the shift of LSPRs toward lower wavelengths with increasing carrier concentration is qualitatively valid. When Fe is codoped with 10% Sn into the In_2O_3 NC lattice, the LSPR band intensity decreases and shifts
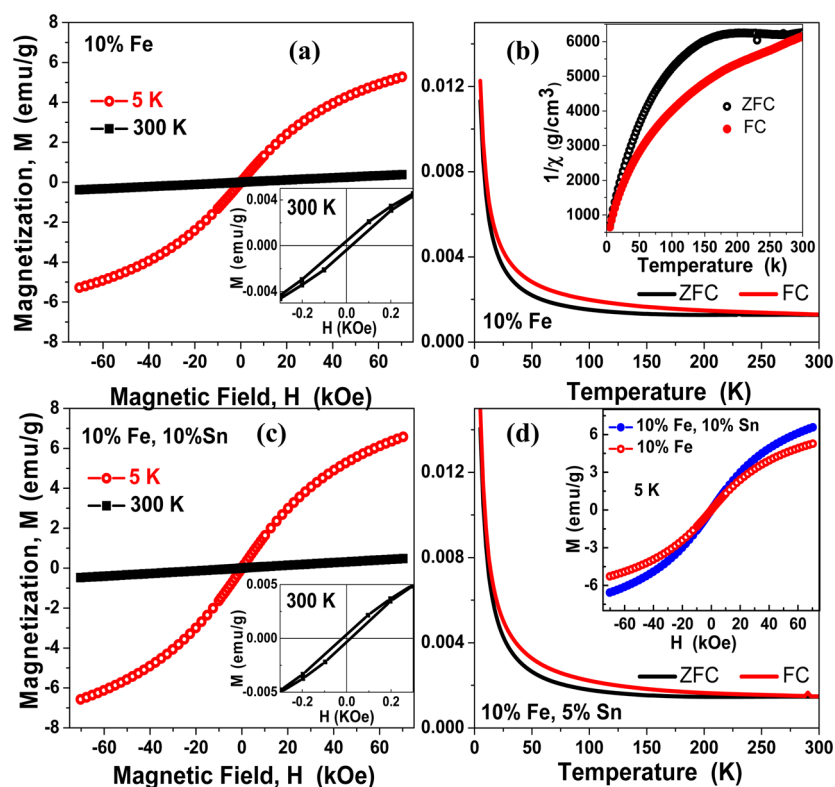
Figure 3. (a) Magnetization (M) vs field (H) plots for 10% Fe-doped In_2O_3 NCs at different temperatures. Inset shows the magnified M vs H plot of the sample at 300 K. (b) ZFC and FC (100 Oe), magnetization (M) vs temperature (T) curves for 10% Fe-doped In_2O_3 NCs. Inset shows the magnetic susceptibility plot corresponding to Curie−Weiss law. (c) Magnetization (M) vs field (H) plots for 10% Fe−10% Sn-codoped In_2O_3 NCs. Inset shows the magnified M vs H plot for 10% Fe−10% Sn-codoped In_2O_3 NCs at 300 K. (d) M vs T curves for 10% Fe−10% Sn-codoped In_2O_3 NCs. Inset compares M vs H data for 10% Fe-doped In_2O_3 NCs with that of 10% Fe−10% Sn-codoped In_2O_3 NCs at 5 K.

toward longer wavelength. Size, shape, structure, and surface capping of NCs are not altered noticeably upon Fe doping. Therefore, the shift in LSPR band can be associated with the Fe^{3+} dopant center. Replacement of In^{3+} with isovalent Fe^{3+} ion in the NC lattice is not expected to influence the carrier concentration, also, a large change in dielectric constant is not expected with <10% Fe doping. A similar increase in LSPR wavelength with increased doping level was observed previously even for heavily doped (typically >10%) ITO NCs because of electron trapping around Sn doping sites.[1,4] A similar kind of electron trapping might also take place in Fe- and Sn-codoped In_2O_3 for heavily doped NCs. Four-probe measurements show resistivity of ~0.4 Ω cm for 10% Fe−10% Sn-codoped sample, significantly higher than that of 10% Sn-doped NCs (<0.1 Ω cm) at room temperature. The resistivity of Fe- and Sn-codoped NCs systematically increase with increasing Fe concentration (0 to 10%), but for a fixed Sn concentration of 10%. These conductivity measurements also suggest trapping/scattering of electrons with Fe doping. Further study is required to have a better understanding about roles of Sn and Fe in controlling the LSPR band. Formation of interstitial or any other kind of defects and partial change in oxidation state of Fe^{3+} in the limit of high doping cannot be ruled out. We note here that the all these NC samples do not absorb visible light. This visible-light transparency makes ITO a preferred electrode material for variety of optoelectronic applications.

On the other hand, high-Curie temperature (T_C) ferromagnetism in transition metal doped dilute magnetic semiconductor (DMS) oxides is an important area of research particularly for spin-based electronic and magneto-optical applications.[20−22] Magnetic properties of DMS NCs were found to depend strongly on interaction between the magnetic dopant and weakly localized or free carriers which can arise from defects or codoping.[23−25] Magnetic properties of bulk and thin films of Fe-doped In_2O_3 obtained by different groups are incongruous. High T_C ferromagnetism was observed in Fe-doped In_2O_3, and it was believed that the ferromagnetism was mediated by mobile electrons that mainly arise from oxygen vacancies.[26−28] In contrast, paramagnetism has been reported[29] from the same system prepared under different conditions. There are only two prior reports of magnetic studies on Fe-doped In_2O_3 NCs, and both suggested weak ferromagnetism at room temperature without forming any impurity phase.[30,31] Film of Cr-doped In_2O_3 nanocrystals also exhibited room temperature ferromagnetism.[32] There are few magnetic studies in both bulk and thin films of Fe- and Sn-codoped In_2O_3,[33] and to the best of our knowledge, there is no prior report on Fe- and Sn-codoped In_2O_3 NCs.

Figure 3a shows magnetization (M) vs magnetic field strength (H) plots for 10% Fe-doped In_2O_3 NCs capped with oleylamine. Clearly, the M vs H plot is nonlinear S-shaped at 5 K but without saturation. Nonlinearity in M vs H is also present at 300 K as shown in magnified data in the inset of Figure 3a. In fact, the inset shows hysteresis at 300 K with small coercivity ~25 Oe. The nonlinear M vs H plots along with weak hysteresis suggest the possibility of weak ferromagnetism at room temperature. The obtained coercivity is about an order of magnitude smaller when compared to bulk samples, although, similar to previous reports of Fe-doped In_2O_3 NCs.[28,31]

Temperature-dependent magnetization (M vs T) for 10% Fe-doped In_2O_3 NCs with zero-field-cooled (ZFC) and field-cooled (FC, 100 Oe) conditions are shown in Figure 3b. There

is a clear divergence between the FC and ZFC even closer to 300 K, which agrees with the weak ferromagnetic hysteresis (inset of Figure 3a) observed at room temperature. Also, there is a paramagnetic-like contribution exhibited by an increasing magnetization at lower temperatures. Inset of Figure 3b shows susceptibility plots for both FC and ZFC data corresponding to Curie−Weiss law, $1/\chi = (T − \theta)/C$, where χ is magnetic susceptibility, C is the Curie constant, T is temperature in K, and θ is the Curie temperature. A linear fit to the Curie−Weiss plots was not possible over a significant temperature range suggesting a complex behavior. We note that the observed M vs T and M vs H plots for our 10% Fe-doped In_2O_3 NCs are similar to prior reports without any major differences.[30,31]

M vs H plots in Figure 3c shows that 10% Fe−10% Sn-codoped In_2O_3 NCs also exhibit qualitatively similar behavior when compared to Figure 3a without the Sn codoping. Inset to Figure 3c also shows a similar coercivity at room temperature. M vs T plots in Figure 3d and the Curie−Weiss plots in Supporting Information Figure S9 for the 10% Fe−10% Sn-codoped In_2O_3 are also qualitatively similar to 10% Fe-doped sample without the Sn codoping. Quantitatively, there is a small increase in magnetization after the codoping with Sn as shown in the inset to Figure 3d and Figure S10 in the Supporting Information. Sn doping provides mobile electrons in conduction band. The increase in magnetization after codoping with electron donating Sn for the same amount of Fe content might be because of the increase in delocalized electron mediated ferromagnetic interaction in the codoped sample.[34] However, such interactions between Sn and Fe dopants need to be studied further. Also oxygen vacancies can provide delocalized electron in the conduction band of In_2O_3. Our NCs with In-rich surface and prepared under N_2 atmosphere can have oxygen vacancies providing delocalized electrons even in the absence of Sn. Therefore, Sn codoping does not lead to dramatic change in the magnetization; instead, a small increase in magnetization is observed due to an increase in already existing delocalized electrons.

In conclusion, we report here the synthesis of Fe- and Sn-codoped colloidal In_2O_3 NCs. Sn doping provided enough free electrons in the conduction band giving strong LSPR band that can be tuned in NIR to mid-IR region based on the dopant concentrations. On the other hand, Fe-doping yields weak ferromagnetism at room temperature. Codoping the NCs with both Sn and Fe results in a multifunctional NC that can exhibit both magnetic and plasmonic properties. Interestingly, our preliminary results suggest possible interactions between magnetic and plasmonic dopants, which needs to be probed further. Fe doping shifts the LSPR band toward longer wavelengths, and Sn doping enhances magnetization. Combination of NIR plasmonics, magnetism, visible-light transparency, and also large enough electronic conductivity is unique to our codoped NCs. Such combinations of properties may find future applications in localized photothermal therapy and spin-based devices.

■ METHODS SECTION

Colloidal syntheses of doped and undoped In_2O_3 nanocrystals (NCs) were carried out using simple single-step strategy. Required stoichiometric amounts of Sn, Fe, and In precursors were used for a given target composition of the NC. For example, in order to synthesize, 10% Fe−10% Sn-codoped In_2O_3 NCs, we mixed 0.243 mmol indium(III) acetylacetonate (Sigma-Aldrich, purity ≥99.9%), 0.030 mmol iron(III)

acetylacetonate (Sigma-Aldrich, purity ≥99.9%), and 0.030 mmol tin(IV) bis(acetylacetonate) dichloride (Sigma-Aldrich, purity 98%) in 10 mL of oleylamine (Sigma-Aldrich, purity 70%) in a 50 mL three-necked round-bottom flask. The mixture was first degassed at room temperature for 20 min by alternatively flushing with vacuum and N_2 gas, and then kept under vacuum conditions for 30 min at 100 °C. The temperature of the reaction mixture was then increased slowly to 220 °C maintaining N_2 gas atmosphere. The reaction is continued for 5 h at 220 °C. Color of the solution slowly changed from brownish-yellow to deep blue during the synthesis. Color of colloidal NCs depends on the composition of the NCs. Fe-doped NCs exhibit light yellow color; however, an increase in Sn doping makes the color blue owing to the tail of the LSPR band extending in the red-end of the visible region. The solution was then cooled to room temperature and added excess methanol as nonsolvent precipitating the NCs, followed by centrifugation at 6000 rpm for 5 min. The NCs obtained were redispersed in toluene and again precipitated using a nonsolvent. The process was repeated thrice. The final oleylamine capped NCs can be redispersed in a suitable nonpolar solvent.

UV−vis−NIR absorption spectra of colloidal NCs dispersed in tetrachloroethylene were recorded using PerkinElmer, Lambda-950 UV/vis spectrometer. TEM data were obtained using a JEOL JEM 2100F microscope operated at 200 kV. Powder XRD patterns of the NCs were obtained using Bruker D8 Advance X-ray diffractometer using Cu Kα as X-ray source. Four probe conductivity measurements were carried out using Keithley Four-Probe Conductivity Instrument (Model 6220/6221 Current Source and Model 2182A nanovoltmeter). Pellets made from NC powder were used for the conductivity measurements. SEM and EDAX data were obtained using Zeiss Ultra Plus SEM Instrument. ICP-OES was carried out using Perkin−Elmer Optima 7000 DV machine. Magnetic properties were measured using SQUID magnetometer (Quantum Design MPMS XL-7 Magnetometer). Zero-field-cooled (ZFC) and field-cooled (FC) data were measured in the temperature range of 5−300 K at magnetic field, $H = 100$ Oe after cooling the amples in zero field or in a 100 Oe field, respectively.

ASSOCIATED CONTENT

Ⓢ Supporting Information

Powder XRD, TEM, SEM, optical absorption and magnetic data are shown. This material is available free of charge via the Internet at http://pubs.acs.org.

AUTHOR INFORMATION

Corresponding Author

*E-mail: angshuman@iiserpune.ac.in.

Notes

The authors declare no competing financial interest.

ACKNOWLEDGMENTS

REFERENCES

(1) Kanehara, M.; Koike, H.; Yoshinaga, T.; Teranishi, T. Indium Tin Oxide Nanoparticles with Compositionally Tunable Surface Plasmon Resonance Frequencies in the Near-IR Region. *J. Am. Chem. Soc.* **2009**, *131*, 17736−17737.

(2) Garcia, G.; Buonsanti, R.; Runnerstrom, E. L.; Mendelsberg, R. J.; Llordes, A.; Anders, A.; Richardson, T. J.; Milliron, D. J. Dynamically Modulating the Surface Plasmon Resonance of Doped Semiconductor Nanocrystals. *Nano Lett.* **2011**, *11*, 4415−4420.

(3) Li, S. Q.; Guo, P. J.; Zhang, L. X.; Zhou, W.; Odom, T. W.; Seideman, T.; Ketterson, J. B.; Chang, R. P. H. Infrared Plasmonics with Indium-Tin-Oxide Nanorod Arrays. *ACS Nano* **2011**, *5*, 9161−9170.

(4) Wang, T.; Radovanovic, P. V. Free Electron Concentration in Colloidal Indium Tin Oxide Nanocrystals Determined by Their Size and Structure. *J. Phys. Chem. C* **2011**, *115*, 406−413.

(5) Lounis, S. D.; Runnerstrom, E. L.; Llordes, A.; Milliron, D. J. Defect Chemistry and Plasmon Physics of Colloidal Metal Oxide Nanocrystals. *J. Phys. Chem. Lett.* **2014**, *5*, 1564−1574.

(6) Nag, A.; Kundu, J.; Hazarika, A. Seeded-Growth, Nanocrystal-Fusion, Ion -Exchange and Inorganic -Ligand Mediated Formation of semiconductor Based Colloidal Heterostructured Nanocrystals. *CrystEngComm* **2014**, DOI: 10.1039/C4CE00462K.

(7) Son, J. S.; Lee, J. S.; Shevchenko, E. V.; Talapin, D. V. Magnet-in-the-Semiconductor Nanomaterials: High Electron Mobility in All-Inorganic Arrays of FePt/CdSe and FePt/CdS Core-Shell Hetero-structures. *J. Phys. Chem. Lett.* **2013**, *4*, 1918−1923.

(8) Santra, P. K.; Kamat, P. V. Tandem-Layered Quantum Dot Solar Cells: Tuning the Photovoltaic Response with Luminescent Ternary Cadmium Chalcogenides. *J. Am. Chem. Soc.* **2013**, *135*, 877−885.

(9) Kim, J.; Park, S.; Lee, J. E.; Jin, S. M.; Lee, J. H.; Lee, I. S.; Yang, I.; Kim, J. S.; Kim, S. K.; Cho, M. H.; et al. Designed fabrication of multifunctional magnetic gold nanoshells and their application to magnetic resonance imaging and photothermal therapy. *Angew. Chem., Int. Ed.* **2006**, *45*, 7754−7758.

(10) Bardhan, R.; Chen, W. X.; Perez-Torres, C.; Bartels, M.; Huschka, R. M.; Zhao, L. L.; Morosan, E.; Pautler, R. G.; Joshi, A.; Halas, N. J. Nanoshells with Targeted Simultaneous Enhancement of Magnetic and Optical Imaging and Photothermal Therapeutic Response. *Adv. Funct. Mater.* **2009**, *19*, 3901−3909.

(11) Dong, W. J.; Li, Y. S.; Niu, D. C.; Ma, Z.; Gu, J. L.; Chen, Y.; Zhao, W. R.; Liu, X. H.; Liu, C. S.; Shi, J. L. Facile Synthesis of Monodisperse Superparamagnetic Fe_3O_4 Core@hybrid@Au Shell Nanocomposite for Bimodal Imaging and Photothermal Therapy. *Adv. Mater.* **2011**, *23*, 5392−5397.

(12) Tian, Q. W.; Hu, J. Q.; Zhu, Y. H.; Zou, R. J.; Chen, Z. G.; Yang, S. P.; Li, R. W.; Su, Q. Q.; Han, Y.; Liu, X. G. Sub-10 nm Fe_3O_4@$Cu_{2-x}S$ Core-Shell Nanoparticles for Dual-Modal Imaging and Photothermal Therapy. *J. Am. Chem. Soc.* **2013**, *135*, 8571−8577.

(13) Faucheaux, J. A.; Stanton, A. L. D.; Jain, P. K. Plasmon Resonances of Semiconductor Nanocrystals: Physical Principles and New Opportunities. *J. Phys. Chem. Lett.* **2014**, *5*, 976−985.

(14) Zhou, T.; Wei, L.; Xie, Y. R.; Li, Q. H.; Hu, G. X.; Chen, Y. X.; Yan, S. S.; Liu, G. L.; Mei, L. M.; Jiao, J. Effects of Sn doping on the morphology and properties of Fe-doped In_2O_3 epitaxial films. *Nanoscale Res. Lett.* **2012**, *7*, 661.

(15) Gilstrap, R. A.; Capozzi, C. J.; Carson, C. G.; Gerhardt, R. A.; Summers, C. J. Synthesis of a Nonagglomerated Indium Tin Oxide Nanoparticle Dispersion. *Adv. Mater.* **2008**, *20*, 4163−4166.

(16) King, P. D. C.; Veal, T. D.; Fuchs, F.; Wang, C. Y.; Payne, D. J.; Bourlange, A.; Zhang, H.; Bell, G. R.; Cimalla, V.; Ambacher, O.; et al. Band gap, electronic structure, and surface electron accumulation of cubic and rhombohedral In_2O_3. *Phys. Rev. B: Condens. Matter Mater. Phys.* **2009**, *79*, 205211.

(17) Shim, M.; Guyot-Sionnest, P. Organic-capped ZnO nanocrystals: Synthesis and n-type character. *J. Am. Chem. Soc.* **2001**, *123*, 11651−11654.

(18) Faucheaux, J. A.; Jain, K. Plasmons in Photocharged ZnO Nanocrystals Revealing the Nature of Charge Dynamics. *J. Phys. Chem. Lett.* **2013**, *4*, 3024−3030.

(19) Schimpf, A. M.; Thakkar, N.; Gunthardt, C. E.; Masiello, D. J.; Gamelin, D. R. Charge-Tunable Quantum Plasmons in Colloidal Semiconductor Nanocrystals. *ACS Nano* **2014**, *8*, 1065−1072.

(20) Dietl, T.; Ohno, H.; Matsukura, F.; Cibert, J.; Ferrand, D. Zener model description of ferromagnetism in zinc-blende magnetic semiconductors. *Science* **2000**, *287*, 1019−1022.

(21) Yu, J. H.; Liu, X. Y.; Kweon, K. E.; Joo, J.; Park, J.; Ko, K. T.; Lee, D.; Shen, S. P.; Tivakornsasithorn, K.; Son, J. S.; et al. Giant Zeeman splitting in nucleation-controlled doped CdSe:Mn2+ quantum nanoribbons. *Nat. Mater.* **2010**, *9*, 47−53.

(22) Viswanatha, R.; Naveh, D.; Chelikowsky, J. R.; Kronik, L.; Sarma, D. D. Magnetic Properties of Fe/Cu Codoped ZnO Nanocrystals. *J. Phys. Chem. Lett.* **2012**, *3*, 2009−2014.

(23) Sapra, S.; Sarma, D. D.; Sanvito, S.; Hill, N. A. Influence of quantum confinement on the electronic and magnetic properties of (Ga,Mn)As diluted magnetic semiconductor. *Nano Lett.* **2002**, *2*, 605−608.

(24) Kittilstved, K. R.; Gamelin, D. R. Activation of high-T_c ferromagnetism in Mn^{2+}-doped ZnO using amines. *J. Am. Chem. Soc.* **2005**, *127*, 5292−5293.

(25) Zheng, W. W.; Strouse, G. F. Involvement of Carriers in the Size-Dependent Magnetic Exchange for Mn:CdSe Quantum Dots. *J. Am. Chem. Soc.* **2011**, *133*, 7482−7489.

(26) Yoo, Y. K.; Xue, Q.; Lee, H. C.; Cheng, S. F.; Xiang, X. D.; Dionne, G. F.; Xu, S. F.; He, J.; Chu, Y. S.; Preite, S. D.; et al. Bulk synthesis and high-temperature ferromagnetism of $(In_{1-x}Fe_x)_2O_3$-sigma with Cu co-doping. *Appl. Phys. Lett.* **2005**, *86*, 042506.

(27) Jayakumar, O. D.; Gopalakrishnan, I. K.; Kulshreshtha, S. K.; Gupta, A.; Rao, K. V.; Louzguine-Luzgin, D. V.; Inoue, A.; Glans, P. A.; Guo, J. H.; Samanta, K.; et al. Structural and magnetic properties of $(In_{1-x}Fe_x)_2O_3$ $(0.0 \leq x \leq 0.25)$ system: Prepared by gel combustion method. *Appl. Phys. Lett.* **2007**, *91*, 052504.

(28) Jiang, F. X.; Xu, X. H.; Zhang, J.; Fan, X. C.; Wu, H. S.; Alshammari, M.; Feng, Q.; Blythe, H. J.; Score, D. S.; Addison, K.; Al-Qahtani, M.; Gehring, G. A. Room temperature ferromagnetism in metallic and insulating $(In_{1-x}Fe_x)_2O_3$ thin films. *J. Appl. Phys.* **2011**, *109*, 053907.

(29) Berardan, D.; Guilmeau, E. Magnetic properties of bulk Fe-doped indium oxide. *J. Phys.: Condens. Matter* **2007**, *19*, 236224.

(30) Chu, D.; Zeng, Y. P.; Jiang, D.; Ren, Z. Tuning the crystal structure and magnetic properties of Fe doped In_2O_3 nanocrystals. *Appl. Phys. Lett.* **2007**, *91*, 262503.

(31) Singhal, A.; Achary, S. N.; Manjanna, J.; Jayakumar, O. D.; Kadam, R. M.; Tyagi, A. K. Colloidal Fe-Doped Indium Oxide Nanoparticles: Facile Synthesis, Structural, and Magnetic Properties. *J. Phys. Chem. C* **2009**, *113*, 3600−3606.

(32) Tarvid, S. S.; Ju, L.; Worden, M.; Radovanovic, P. V. Colloidal Chromium-Doped In_2O_3 Nanocrystals as Building Blocks for High-T-C Ferromagnetic Transparent Conducting Oxide Structures. *J. Phys. Chem. C* **2008**, *112* (46), 17755−17759.

(33) Venkatesan, M.; Gunning, R. D.; Stamenov, P.; Coey, J. M. D. Room temperature ferromagnetism in Mn- and Fe-doped indium tin oxide thin films. *J. Appl. Phys.* **2008**, *103*, 07D135.

(34) Yu, Z. G.; He, J.; Xu, S. F.; Xue, Q. Z.; van't Erve, O. M. J.; Jonker, B. T.; Marcus, M. A.; Yoo, Y. K.; Cheng, S. F.; Xiang, X. D. Origin of ferromagnetism in semiconducting $(In_{(1-x-y)}Fe_xCu_y)_2O_3$ sigma. *Phys. Rev. B: Condens. Matter Mater. Phys.* **2006**, *74*, 254214.